3D chemo-mechanical modeling of microstructure evolution and anisotropic deformation in $\mathrm{Na}_x\mathrm{V}_2(\mathrm{PO}_4)_3$ cathode particles for sodium-ion batteries

Tao Zhang[a,*], Mohsen Sotoudeh[b], Xiaohu Yao[a], Axel Groß[b,c], Marc Kamlah[d]

[a]*School of Civil Engineering and Transportation, South China University of Technology, Guangzhou 510640, China*
[b]*Institute of Theoretical Chemistry, Ulm University, 89069 Ulm, Germany*
[c]*Helmholtz Institute Ulm (HIU), Electrochemical Energy Storage, 89069 Ulm, Germany*
[d]*Institute for Applied Materials, Karlsruhe Institute of Technology, 76344 Eggenstein-Leopoldshafen, Germany*

Abstract

The cathode material $\mathrm{Na}_x\mathrm{V}_2(\mathrm{PO}_4)_3$ of sodium-ion batteries displays complicate phase segregation thermodynamics with anisotropic deformation during (de)intercalation. A virtual multiscale modeling chain is established to develop a 3D anisotropic chemo-mechanical phase-field model based on first-principles calculations for $\mathrm{Na}_x\mathrm{V}_2(\mathrm{PO}_4)_3$. This model accounts for diffusion, phase changes, anisotropic misfit strain, and anisotropic elasticity. The multiwell potential of $\mathrm{Na}_x\mathrm{V}_2(\mathrm{PO}_4)_3$ is constructed, which captures phase segregation into a sodium-poor phase $\mathrm{NaV}_2(\mathrm{PO}_4)_3$ and a sodium-rich phase $\mathrm{Na}_3\mathrm{V}_2(\mathrm{PO}_4)_3$. The elastic properties of $\mathrm{NaV}_2(\mathrm{PO}_4)_3$ are determined by first-principles for the first time. Furthermore, we address how elastic effects and crystal orientation influence the full 3D microstructure evolution, including

---

*Corresponding author.
Email address: taozhang@scut.edu.cn (Tao Zhang)

phase evolution, interface morphology, and stress evolution in $Na_xV_2(PO_4)_3$ particles. We find that the quasi-equilibrium single wave propagation along [010] is determined by the anisotropic elasticity tensor. The anti-orthotropic symmetry property of the elasticity tensor leads to the striking behavior of warping of the interface. Furthermore, the phase boundary motion is thermodynamically affected by the crystal orientation, which is controlled by minimization of the interface area. It is found that the [010] crystal orientation is mechanically more reliable and recommended for $Na_xV_2(PO_4)_3$ electrode design. Apart from yielding information about the properties of $Na_xV_2(PO_4)_3$, the findings of this work may offer an opportunity to achieve improved mechanical stability of the phase separating electrode materials by engineering the crystal orientation.

1. Introduction

Sodium-ion batteries (NIBs) are regarded as a promising alternative to lithium-ion batteries (LIBs) due to the wide availability, low cost of sodium, and comparable energy density (Buchholz et al., 2013; Dou et al., 2019; Vaalma et al., 2018). $Na_xV_2(PO_4)_3$, which has a NASICON (Na Super Ionic Conductor)-type framework, is one of the most important cathode materials for NIBs due to its excellent ionic conductivity, high voltage plateau located at 3.4 V, high theoretical specific capacity, and thermal stability (Akcay et al., 2021; Jian et al., 2013, 2014; Lim et al., 2012; Pandit et al., 2024; Stüble et al., 2024). It should be noticed that $Na_xV_2(PO_4)_3$ also exhibits a voltage plateau

at 1.6 V, which suggests its potential as a promising anode material (Akcay et al., 2021; Jian et al., 2012; Song et al., 2014), but we focus on the cathode function of $Na_xV_2(PO_4)_3$ in this work. According to first principle calculations (Lim et al., 2012), if all Na sites were occupied by Na ions in each formula unit of $Na_xV_2(PO_4)_3$, four cations could be completely hosted: one surrounded by six oxygen atoms (Na1 site) and three surrounded by eight oxygen atoms (Na2 sites). However, due to the relatively unstable state of V^{2+} in $Na_4V_2(PO_4)_3$, it is more favorable to synthesize $Na_3V_2(PO_4)_3$, as V^{3+} is in a more stable oxidation state. In the crystal structure of $Na_3V_2(PO_4)_3$, one Na ion occupies the Na1 site (1.0 occupancy) and two Na ions occupy Na2 sites (0.67 occupancy) (Jian et al., 2014; Lim et al., 2012). Upon sodium intercalation, both in situ XRD measurement (Jian et al., 2013) and DFT calculations (Lim et al., 2012) indicate that $Na_xV_2(PO_4)_3$ ($1 < x < 3$) undergoes a two-phase reaction between $NaV_2(PO_4)_3$ and $Na_3V_2(PO_4)_3$ with a volume mismatch of 8.26 %.

For phase separating cathode materials, lattices deform abruptly and anisotropically when species are inserted into the storage material. The respective phases has different lattice constants, leading to large concentration gradients and thus significant stress magnitudes. These phenomena would cause particle cracking, structural decay of storage materials, and battery capacity loss (Bistri and Di Leo, 2023; Chang et al., 2018; Di Leo et al., 2015; Ganser et al., 2019; Huang et al., 2022; Huang and Guo, 2024; Klinsmann et al., 2016a,b; Li et al., 2019; Wang et al., 2021; Xu et al., 2019; Zhang et al., 2020). For thermodynamical reasons, there is a contribution of the stresses to the driving force for diffusion and phase changes in the storage material

3

(Deshpande and McMeeking, 2023; Jiang and Zhong, 2023; Zhang and Kamlah, 2019). The chemo-mechanical coupling plays a nontrivial role in the degradation mechanisms of the battery, and has attracted considerable attention in the battery community. For example, an electro-chemo-mechanical fracture model of species diffusion, ionic conduction, interfacial reaction, mechanical stress, and crack growth has been recently developed for storage particles embedded in the solid electrolyte in cathodes of solid-state batteries to investigate defect-initiated interface delamination and how cracks nucleate in electrolytes in a full 3D dynamical description for the first time (Zhang et al., 2024a). It has been found that unstable interface delamination very likely happens during charging, the electrolyte can break into several parts within a single insertion half-cycle, and can even be completely comminuted for larger particle sizes and higher applied current densities. It is thus important to understand how phase separation of $Na_xV_2(PO_4)_3$ interacts with the stresses and how this interplay, in turn, governs the macroscopic material response such as micro-cracking. To the best of our knowledge, neither experimental nor theoretical studies have revealed how the microstructure of the phase separation, including phase evolution and interface morphology, as well as the stresses evolve for $Na_xV_2(PO_4)_3$.

The description of the complex thermodynamics of phase segregation along with the structural change that occurs in $Na_xV_2(PO_4)_3$ and the elucidation of the interaction between microstructure evolution and mechanics represent severe challenges for any modeling approach. Thermodynamic phase-field modeling can provide a consistent and accurate approach describing phase changes accompanied by diffusion. A Cahn-Hilliard type phase-

4

field method (Cahn and Hilliard, 1958), which is weakly nonlocal (Zhang and Kamlah, 2018a), employs species composition (e.g., Na-ion) as the continuous order parameter, leading to diffuse interfaces between phases without the troublesome tracking of the sharp interface position (Afshar and Di Leo, 2021; Di Leo et al., 2014). Besides the phase field models that describe phase changes in intercalation materials as a function of concentration alone, a thermodynamically consistent phase-field theory (Zhang et al., 2024b), which couples the Cahn-Hilliard type diffusion with the finite deformation of host lattices governed by nonlinear gradient elasticity, was recently derived based on the principle of virtual power and the second law of thermodynamics. This multiscale theoretical framework is applied for the cathode material $Li_2Mn_2O_4$ to investigate the interplay between diffusion and the cubic-to-tetragonal deformation of lattices during insertion. The simulation results provide quantitative insights into the nucleation and growth of twinned microstructures during discharging. This theoretical framework not only depends on the concentration order parameter but also on the strain order parameter to capture the coupling between the diffusion of a guest species at the continuum scale and finite deformation of host lattices at the atomic scale for symmetry-lowering intercalation materials.

For NIBs, although many intercalation electrode materials exhibit phase separation, chemo-mechanical phase-field models have been almost entirely focused on Na_xFePO_4 (Zhang and Kamlah, 2018b, 2020, 2021; Zhang et al., 2023). A mechanically coupled phase-field model was developed for a spherically symmetric boundary value problem of Na_xFePO_4 (Zhang and Kamlah, 2018b). Subsequently, a 2D chemo-mechanical phase-field model for

5

Na$_x$FePO$_4$ was developed, including both, the two phase segregation between FePO$_4$ and Na$_{2/3}$FePO$_4$, as well as the solid-solution phase Na$_x$FePO$_4$ ($2/3 < x < 1$) (Zhang and Kamlah, 2021). It was found that the intermediate phase leads to varying solubility limits and lower magnitudes of sodiation stress. Recently, four different phase-separating dynamical processes are captured in 3D storage particles of Na$_x$FePO$_4$ (Zhang et al., 2023). It is necessary to perform full 3D simulations with the appropriate crystal anisotropy to study the complex phase morphologies observed in experiments. To the best of our knowledge, no studies have explored the chemo-mechanical phase-field modeling of Na$_x$V$_2$(PO$_4$)$_3$ regarding the interaction between microstructure evolution and mechanics. The concept of the virtual multiscale modeling chain, which combines an anisotropic chemo-mechanical phase-field model and DFT calculations, can be applied to Na$_x$V$_2$(PO$_4$)$_3$ to study 3D phase evolution, anisotropic phase boundary morphologies, and stress generation in 3D.

In this work, a virtual multiscale modeling chain is established to develop a 3D anisotropic chemo-mechanical phase-field model based on first-principles calculations for Na$_x$V$_2$(PO$_4$)$_3$, accounting for diffusion, phase nucleation and spinodal decomposition, anisotropic misfit strain, as well as anisotropic elasticity. Currently, no experimental data is available for the elastic properties of Na$_x$V$_2$(PO$_4$)$_3$. The elastic properties of NaV$_2$(PO$_4$)$_3$ are calculated from DFT for the first time. Furthermore, based on the experimental open circuit voltage, a multiwell potential is determined for Na$_x$V$_2$(PO$_4$)$_3$, accounting for two-phase segregation between NaV$_2$(PO$_4$)$_3$ and Na$_3$V$_2$(PO$_4$)$_3$. We study how elastic effects and crystal orientation af-

fect the full 3D microstructure evolution of $Na_xV_2(PO_4)_3$. We envision that improved mechanical stability, and thus better battery performance of the phase separating electrode materials may be achieved by engineering the crystal orientation.

2. Methods

2.1. A virtual multiscale modeling chain

2.1.1. First-principles calculations

We carried out first-principles calculations based on density-functional theory (DFT) (Euchner and Groß, 2022; Hohenberg and Kohn, 1964; Kohn and Sham, 1965), and implemented the Projector Augmented Wave (PAW) method (Blöchl, 1994) in the Vienna *Ab-initio* Simulation Package (VASP) (Kresse and Furthmüller, 1996; Kresse and Hafner, 1993; Kresse and Joubert, 1999). The exchange-correlation effects were treated using the generalized gradient approximation (GGA) with the Perdew-Burke-Ernzerho (PBE) functional (Perdew et al., 1996). To accurately capture the behavior of the localized d-electrons in the system, Hubbard U parameters (Wang et al., 2006) were applied. Specifically, $U_V = 3.25$ eV was chosen for V atoms in $NaV_2(PO_4)_3$. Calculations were optimized using a $2\times2\times2$ k-point mesh with a plane-wave cutoff energy of 520 eV, ensuring convergence to within 1×10^{-5} eV per supercell. The atomic positions and cell volume were fully relaxed without constraints.

$NaV_2(PO_4)_3$ was modeled in its rhombohedral structure with an $R\bar{3}c$ space group, where the vanadium ions occupy octahedral sites surrounded by oxygen atoms, while phosphate groups separate the octahedrons. For all

7

simulations, a ferromagnetic configuration was used for the magnetic ground-state structure. Symmetric distortion matrices were applied to the equilibrium unit cell of $NaV_2(PO_4)_3$ to calculate the elastic constants. The time step for ionic motion was set to 0.0075 to minimize higher-order contributions to the elastic constants.

The shear modulus G, bulk modulus K, and Young's modulus E were derived from the calculated elastic constants c_{ij} $(i, j = 1, \ldots, 6)$ using the Voigt, Reuss, and Hill approximations. According to Voigt's approximation, the shear and bulk moduli are expresses as

$$
\begin{aligned}
G_V &= \frac{1}{15}(c_{11} + c_{22} + c_{33} - c_{12} - c_{13} - c_{23}) + \\
&\quad \frac{1}{5}(c_{44} + c_{55} + c_{66}),
\end{aligned} \tag{1}
$$

$$
K_V = \frac{1}{9}(c_{11} + c_{22} + c_{33}) + \frac{2}{9}(c_{12} + c_{13} + c_{23}). \tag{2}
$$

Based on the Reuss approximation, the shear and bulk moduli are given by

$$
G_R = \frac{1}{4(s_{11} + s_{22} + s_{33}) - 4(s_{12} + s_{13} + s_{23}) + 3(s_{44} + s_{55} + s_{66})}, \tag{3}
$$

$$
K_R = \frac{1}{(s_{11} + s_{22} + s_{33}) + 2(s_{12} + s_{13} + s_{23})}, \tag{4}
$$

where the compliance tensor $\mathbf{S}$ is the inverse of the elasticity tensor, $\mathbf{S} = \mathbf{C}^{-1}$.

The Voigt and Reuss approximations represent the upper and lower bounds of the polycrystalline moduli. Hill's approximation provides the mean

8

values of these moduli as

$$K_H = \frac{1}{2}(KG_R + G_V), \ G_H = \frac{1}{2}(K_R + K_V). \tag{5}$$

Finally, Poisson's ratio ν and Young's modulus E are determined by

$$\nu = \frac{3K - 2G}{2(3K + G)}, \tag{6}$$

$$E = \frac{9KG}{3K + G}. \tag{7}$$

2.1.2. Anisotropic chemo-mechanical phase-field model

We propose an anisotropic chemo-mechanical model for $Na_xV_2(PO_4)_3$, where the normalized sodium concentration $\bar{c}$ scaled with the maximum sodium concentration c_{max} is introduced as an order parameter. The system free energy is

$$\Psi(c, \text{grad}\,c, \boldsymbol{\varepsilon}) = \int_{\mathcal{B}} \left(\psi^{mwp}(c) + \psi^{gd}(\text{grad}\,c) + \psi^e(c, \boldsymbol{\varepsilon}) \right) dV, \tag{8}$$

where the multiwell potential ψ^{mwp} defines the respective phases, constructed by

$$\begin{aligned}
\psi^{mwp} =\ & RT_{ref}c_{max} \left(\bar{\mu}^0\bar{c} + \frac{T}{T_{ref}} \left(\bar{c}\ln\bar{c} + (1 - \bar{c})\ln(1 - \bar{c}) \right) \right. \\
& \left. + \bar{c}(1 - \bar{c})\sum_{i=1}^{n} \alpha_i(1 - 2\bar{c})^{i-1} \right).
\end{aligned} \tag{9}$$

Here, R and T_{ref} are universal gas constant and reference temperature, respectively. The reference chemical potential (Hörmann and Groß, 2019) is described by the first term on the right-hand side of Equation (9), and the terms related to T stand for the entropy of mixing. The Redlich-Kister equation (Redlich and Kister, 1948) is employed to represent the enthalpic

9

effect, and the weight of enthalpy is described by the coefficients α_i. We will determine the above unknown parameters by fitting the experimental open-circuit voltage to capture the two-phase segregation between $\mathrm{NaV_2(PO_4)_3}$ and $\mathrm{Na_3V_2(PO_4)_3}$. The gradient energy density leading to a diffuse interface between phases is given by (Cahn and Hilliard, 1958)

$$\psi^{gd} = RT_{ref}c_{max}\left(\frac{1}{2}\lambda|\operatorname{grad}\bar{c}|^2\right). \tag{10}$$

Here, λ is a material constant with units of length squared. The elastic strain energy density ψ^e, which is also called the coupling energy density, is expressed as

$$\psi^e = \frac{1}{2}\left(\boldsymbol{\varepsilon} - \boldsymbol{\varepsilon^s}\right) : \mathbf{C} : \left(\boldsymbol{\varepsilon} - \boldsymbol{\varepsilon^s}\right), \tag{11}$$

where the total strain tensor $\boldsymbol{\varepsilon}$ is

$$\varepsilon_{ij} = \frac{1}{2}\left(u_{i,j} + u_{j,i}\right) \tag{12}$$

with u_i being the displacement vector. Here, $\mathbf{C}$ represents anisotropic elasticity, which is determined by first-principles. The concentration-dependent stress-free strain $\boldsymbol{\varepsilon^s}$ is given by

$$\boldsymbol{\varepsilon^s} = (\bar{c} - \bar{c}_0)\boldsymbol{\varepsilon^0}, \tag{13}$$

where $\bar{c}_0$ is the normalized initial sodium concentration, and $\boldsymbol{\varepsilon^0}$ is the anisotropic misfit strain.

With the elastic strain energy density, the constitutive relations are computed through functional derivatives, yielding the stress tensor

$$\mathbf{T} = \frac{\partial\psi^e}{\partial\boldsymbol{\varepsilon}} = \mathbf{C} : \left(\boldsymbol{\varepsilon} - (\bar{c} - \bar{c}_0)\boldsymbol{\varepsilon^0}\right). \tag{14}$$

10

The variation $\delta\Psi(c, \operatorname{grad} c, \boldsymbol{\varepsilon})$ with respect to the sodium concentration,

$$
\begin{aligned}
\delta\Psi(c, \operatorname{grad} c, \boldsymbol{\varepsilon}) \quad = \quad & \int_{\mathcal{B}} dV \left(\frac{\partial \psi^{mwp}}{\partial c} - RT_{ref}\lambda \operatorname{div}(\operatorname{grad}\bar{c}) - \frac{1}{c_{max}}\boldsymbol{\varepsilon}^{\mathbf{0}} : \mathbf{T} \right) \delta c \\
& + \int_{\partial\mathcal{B}} dA \frac{RT_{ref}}{c_{max}}\lambda \operatorname{grad} c \cdot \vec{n}\delta c,
\end{aligned} \tag{15}
$$

yields the chemical potential

$$
\begin{aligned}
\mu \quad = \quad & \frac{\delta\Psi}{\delta c} \\
= \quad & \frac{\partial \psi^{mwp}}{\partial c} - RT_{ref}\lambda \operatorname{div}(\operatorname{grad}\bar{c}) - \frac{1}{c_{max}}\boldsymbol{\varepsilon}^{\mathbf{0}} : \mathbf{T},
\end{aligned} \tag{16}
$$

which is the driving force for diffusion and phase changes, as well as the natural boundary condition

$$
\operatorname{grad} c \cdot \vec{n} = 0, \tag{17}
$$

which guarantees that the interface is perpendicular to the particle surface (Cogswell and Bazant, 2012).

The amount of Na per reference volume flowing with a certain velocity of Na atoms $\vec{v}_{Na}$ defines the mass flux

$$
\vec{J} = -c\mathbf{M} \cdot \operatorname{grad}\mu, \tag{18}
$$

and we choose a concentration-dependent mobility tensor

$$
\mathbf{M}(c) = \frac{D_0(c_{max} - c)}{RT_{ref}c_{max}}\mathbf{I}, \tag{19}
$$

with the diffusion coefficient D_0.

Finally, the field equations are obtained from the balances of mass and linear momentum, respectively,

$$
\frac{\partial c}{\partial t} = \operatorname{div}(c\mathbf{M}(c)\operatorname{grad}\mu), \tag{20}
$$

11

$$\operatorname{div} \mathbf{T} = \vec{0}. \tag{21}$$

Equation (20) is the mechanically coupled Cahn-Hilliard diffusion equation, and mechanical equilibrium is represented by Equation (21). Based on the constitutive equations introduced above, a system of partial differential equations (PDEs) is formed from the field equations for concentration and displacement vector. We need the initial and boundary conditions to solve this fourth-order nonlinear initial-boundary-value problem.

For the diffusion, a mass flux at the surface is chosen as

$$\vec{J} \cdot \vec{n} = \begin{cases} -\frac{C c_{max} V}{3600 \cdot S} & \text{for} \quad c \leq c_{max} \\ 0 & \text{for} \quad c = c_{max} \end{cases}, \tag{22}$$

Here, V, S and C are the storage particle volume, the storage particle surface, and the C-rate, respectively. $\vec{n}$ denotes the outgoing unit vector normal to the particle surface.

For the mechanical part, the stress-free state is assumed at the surface,

$$\mathbf{T} \cdot \vec{n} = \vec{0}. \tag{23}$$

2.2. Material parameters and implementation

2.2.1. Construction of the multiwell potential and experimental fitting

In the crystal structure of the sodium-poor phase $NaV_2(PO_4)_3$, one Na ion occupies the Na1 site while no Na ions occupy a Na2 site, resulting in an occupancy of 0.25 occupation for all Na sites. As for the crystal structure of the sodium-rich phase $Na_3V_2(PO_4)_3$, one Na ion occupies the Na1 site and two Na ions occupy the Na2 sites, leading to 0.75 occupation for all Na sites. We will now address how the unknown parameters of the multiwell potential

12

(9) are determined so that the multiwell potential matches the phase segregation thermodynamics of $Na_xV_2(PO_4)_3$.

First, the open circuit voltage E_{oc} is associated with the chemical potential μ by (Birkl et al., 2015)

$$E_{oc}(\bar{c}, T) = -\frac{1}{eN_A}\mu(\bar{c}, T),\tag{24}$$

where the chemical potential μ can be constructed by

$$\mu(\bar{c}, T) = \begin{cases} RT\left(\frac{\bar{\psi}^{mwp}(\bar{c}_{0+}, T) - \bar{\psi}^{mwp}(\bar{c}_{0-}, T)}{\bar{c}_{0+} - \bar{c}_{0-}}\right) & \text{if } \bar{c}_{0-} \leq \bar{c} \leq \bar{c}_{0+} \\ RT\frac{\partial\bar{\psi}^{mwp}}{\partial\bar{c}} & \text{for otherwise} \end{cases}\tag{25}$$

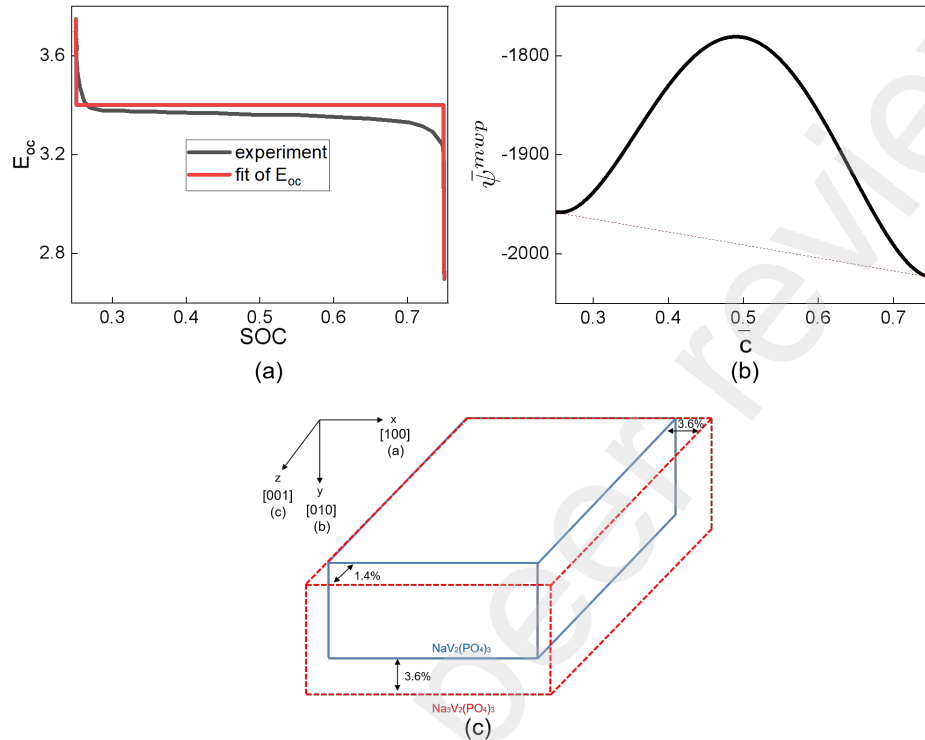Here, the binodal concentrations $\bar{c}_{0-}$ and $\bar{c}_{0+}$ can be found by the Maxwell construction

$$\frac{\partial\bar{\psi}^{mwp}(\bar{c}_{0-})}{\partial\bar{c}} = \frac{\partial\bar{\psi}^{mwp}(\bar{c}_{0+})}{\partial\bar{c}} = \frac{\bar{\psi}^{mwp}(\bar{c}_{0+}) - \bar{\psi}^{mwp}(\bar{c}_{0-})}{\bar{c}_{0+} - \bar{c}_{0-}}\tag{26}$$

that constructs the common tangent to the multiwell potential curve. The free energy density are normalized according to $\bar{\psi} = \psi/(RT_{ref}c_{max})$.

Combining Equations (24) and (25), we fit the open-circuit voltage to the experimental data (Jian et al., 2012) with respect to the unknown parameters. A good fit is achieved with $n = 3, \bar{\mu}^0 = -132.12, \alpha_1 = -6858.7, \alpha_2 = 0$, and $\alpha_3 = -13613$, see Fig. 1a. In line with the experimental data, the fitting voltage plateau is located at 3.4 V, which also matches DFT calculations (Lim et al., 2012). This guarantees that the phase segregation happens at the two binodal concentrations $\bar{c}_{0-} = 0.25$ and $\bar{c}_{0+} = 0.75$.

As shown in Fig. 1b, the dimensionless multiwell potential shows a doublewell structure with two different relative minima at $\bar{c} = 0.25$ and $\bar{c} = 0.75$, characterizing the low concentration phase $NaV_2(PO_4)_3$ and the high

13

concentration phase $Na_3V_2(PO_4)_3$, respectively. The Maxwell construction, which describes the volume fractions of the two phases in phase segregated states, employs a common tangent (see the dashed red line in Fig. 1b) to connect the neighborhoods of the two minima. It should be mentioned that the slope of the Maxwell construction in our constructed multiwell potential curve is consistent with DFT calculations (Lim et al., 2012). The "nucleation zones" is given by the two ranges between the binodal concentrations and the neighboring inflection points. Phase changes is nucleated upon sufficient disturbance of the system. The "spinodal decomposition zone" is defined by the inner zone of concavity between the two inflection points. In this zone, homogeneous concentration is not possible and phase segregation is triggered. Therefore, this constructed multiwell potential captures phase segregation into a sodium-poor phase $NaV_2(PO_4)_3$ and a sodium-rich phase $Na_3V_2(PO_4)_3$.

This preprint research paper has not been peer reviewed. Electronic copy available at: https://ssrn.com/abstract=5087198

Fig. 1. (a) Fit of the open-circuit voltage to the experimental data (Jian et al., 2012). (b) The multiwell potential of $Na_xV_2(PO_4)_3$, where the dashed red line represents the Maxwell construction. (c) Schematic representation of prismatic-like single-crystalline particles of $Na_xV_2(PO_4)_3$ with anisotropic misfit strain between $NaV_2(PO_4)_3$ and $Na_3V_2(PO_4)_3$. For each direction, the corresponding Miller index and space group $Pnma$ axis are shown in parentheses.

2.2.2. The calculated elastic properties

The elastic constants obtained from GGA+U calculations for $NaV_2(PO_4)_3$ are presented in Table 1. To accurately describe the structural properties of $NaV_2(PO_4)_3$, which can behave as a Mott insulator, the Hubbard U correction is applied. While standard GGA calculations often predict metallic

15

behavior for such materials, the U correction significantly improves the description of their insulating nature. The elastic constant c_{22} of $NaV_2(PO_4)_3$ is notably larger than other elastic constants, indicating a significant elastic anisotropy. What is more, $NaV_2(PO_4)_3$ exhibits the anti-orthotropic symmetry property of the elasticity tensor, with non-vanishing magnitudes for c_{16}, c_{26}, c_{36}, as well as c_{45}. The calculated bulk, Young's, and shear moduli, derived from Voigt, Reuss, and Hill averages, are provided in Table 2.

Table 1

The calculated elastic constants (in GPa) of $NaV_2(PO_4)_3$ using GGA+U calculations.

c_{11}	c_{22}	c_{33}	c_{44}	c_{55}	c_{66}	c_{12}
133.36	213.16	165.13	51.45	61.40	46.99	73.25
c_{13}	c_{16}	c_{23}	c_{26}	c_{36}	c_{46}	
34.91	-24.11	89.10	-12.85	-18.76	0.53	

2.3. Implementation

Fig. 1c shows the schematic of a prismatic-like single-crystalline particle of $Na_xV_2(PO_4)_3$ with anisotropic misfit strain between $NaV_2(PO_4)_3$ and $Na_3V_2(PO_4)_3$ (Lim et al., 2012). We consider the insertion of sodium into cathodic particles at a C-rate of 0.01. The material parameters for $Na_xV_2(PO_4)_3$ are summarized in Table 3. It should be noticed that $Na_xV_2(PO_4)_3$ exhibits a three-dimensional sodium ion diffusion channel, leading to isotropy of the mobility (Lim et al., 2012; Song et al., 2014). "State of charge" (SOC) is defined as $SOC = \int_{\mathcal{B}} \bar{c} dV/V$, and $\bar{\Psi}_{avg} = \int_{\mathcal{B}} \bar{\psi} dV/V$ is the normalized average system free energy. Here, Cartesian coordinates are introduced, and

Table 2

The calculated polycrystalline bulk and shear modulus of $NaV_2(PO_4)_3$ in GPa, as well as the Poisson ratio obtained with GGA+U.

Averaging scheme	Bulk modulus	Shear modulus	Poisson's ratio
Voigt	$K_V = 100.69$	$G_V = 115.81$	$\nu_V = 0.08$
Reuss	$K_R = 80.49$	$G_R = 49.02$	$\nu_R = 0.25$
Hill	$K_H = 90.59$	$G_H = 82.42$	$\nu_H = 0.15$

all fields depend on position and time according to

$$c = c(x, y, z, t), \tag{27}$$

$$\vec{u} = u_x(x, y, z, t)\vec{e}_x + u_y(x, y, z, t)\vec{e}_y + u_z(x, y, z, t)\vec{e}_z. \tag{28}$$

Both fourth-order spatial derivatives in concentration and third-order spatial derivatives in displacement are involved in the mechanically coupled Cahn-Hilliard equation (20), such that it is not sufficient for discretization for the standard finite element method with C^0-continuous Lagrange basis functions. To resolve this numerical challenge, the chemical potential is introduced as an additional degree of freedom to split this fourth-order PDE into two second-order equations. The three equations (16), (20), and (21) describe this coupled system with the independent variables c, μ, and $\vec{u}$, respectively. The resulting set of equations is first written in weak form (see Appendix A), and then implemented in the finite-element, multiphysics framework MOOSE (Gaston et al., 2009).

We employ the preconditioned Jacobian Free Newton Krylov (PJFNK) method with a generalized minimal residual method (GMRES) Krylov iterative solver, as well as the Additive Schwarz method (ASM) preconditioner

17

with a LU subsolver to solve the above system of nonlinear equations without the explicit tangent matrix, thereby saving computational time and storage space. We use the implicit Backward-Euler time integration method for time integration. We remove the six 3D rigid body modes at the solver level to avoid arbitrary rigid body displacements and rotations. An adaptive time stepping method is used to handle the initiation of phase nucleation. Simulations are performed on a high-performance Linux computer cluster. 3-D simulations are run on 896 processors and take up to a maximum of 27 days.

3. Results and Discussion

3.1. 3D microstructure evolution

In order to derive trends, in our simulations, we first consider a full 3D single-crystalline particle with cubic morphology of size $L = 500nm$. The system free energy evolution of $\mathrm{Na}_x\mathrm{V}_2(\mathrm{PO}_4)_3$ is shown in Fig. 2 by the solid line, and the evolution of the 3D microstructure and the corresponding maximum principal stress, σ_I, is illustrated in Fig. 3. For comparison, the normalized multiwell potential versus dimensionless concentration is also presented in Fig. 2. The solid line matching the dimensionless multiwell potential curve indicates homogeneous states whereas the solid line nearby the Maxwell construction path corresponds to phase segregated states. Four "kinks" (A-D) are shown in the curve of the system free energy, indicated by a sharp dropping process. We will now look into if there is any relationship between these "kinks" and the microstructure evolution of $\mathrm{Na}_x\mathrm{V}_2(\mathrm{PO}_4)_3$.

Starting from the sodium-poor phase $\mathrm{NaV}_2(\mathrm{PO}_4)_3$, the insertion process

18

Table 3

The material parameters for $\mathrm{Na}_x\mathrm{V}_2(\mathrm{PO}_4)_3$

Parameters	Values
$\bar{\mu}^0$	-132.12
α_1	-6858.7
α_2	0
α_3	-13613
λ	8.2304×10^{-15} (m^2)
D_0	1.02×10^{-15} (m^2/s) (Song et al., 2014)
c_{max}	9.2267×10^3 (mol/m^3) (Du et al., 2013)
$\boldsymbol{\varepsilon^0}$	$\begin{pmatrix} 3.6\% & 0 & 0 \\ 0 & 3.6\% & 0 \\ 0 & 0 & 1.4\% \end{pmatrix}$ (Lim et al., 2012)
$\mathbf{C}$	$\begin{pmatrix} 133.36 & 73.25 & 34.91 & 0 & 0 & -24.11 \\ 73.25 & 213.16 & 89.10 & 0 & 0 & -12.85 \\ 34.91 & 89.10 & 165.13 & 0 & 0 & -18.76 \\ 0 & 0 & 0 & 51.45 & 0.53 & 0 \\ 0 & 0 & 0 & 0.53 & 61.40 & 0 \\ -24.11 & -12.85 & -18.76 & 0 & 0 & 46.99 \end{pmatrix}$ (GPa)

19

initially occurs through a nearly homogeneous filling throughout the particle. Once the SOC approaches 35.645%, the sodium-rich phase $Na_3V_2(PO_4)_3$ first nucleates at the particle corners, and a sodium-rich island quickly forms along the [010] edge. The nucleation reflects itself via the first "kink" A in the curve of the system free energy in Fig. 2. In a very short time, the two sodium-rich islands at the [001] edge coalesce into one individual sodium-rich domain, while other smaller $Na_3V_2(PO_4)_3$ nuclei shrink and disappear, reducing individual sodium-rich islands. The minimization of the total system free energy induces the abrupt appearance of a sodium-rich cylindrical island along [001], see SOC=35.65%. Such expansion anisotropy can be due to the competition between the anisotropic misfit strain and the anisotropic elasticity tensor. The anisotropic misfit strain between $NaV_2(PO_4)_3$ and $Na_3V_2(PO_4)_3$, which is smallest along [001] (1.4%) but along [100] and [010] is 3.6%, favors the nucleation of a sodium-rich cylindrical island along [001]. On the other hand, the anisotropic elasticity tensor favors this nucleation along [100] due to the smallest component of the elasticity tensor in this direction. Thus the anisotropic misfit strain "wins" the competition with the anisotropic elasticity tensor to minimize the elastic strain energy, leading to the abrupt appearance of a sodium-rich cylindrical island along [001]. This is well illustrated through a control simulation, in which we consider an isotropic misfit strain. In this control simulation, we find that a sodium-rich cylindrical island nucleates along [100] determined by the anisotropic elasticity tensor (we do not show this result here). As a result, the elastic strain energy facilitates phase expansion along [001] to decrease stresses. The stresses are mainly located at the interface between the sodium-poor phase

20

$NaV_2(PO_4)_3$ and the sodium-rich phase $Na_3V_2(PO_4)_3$.
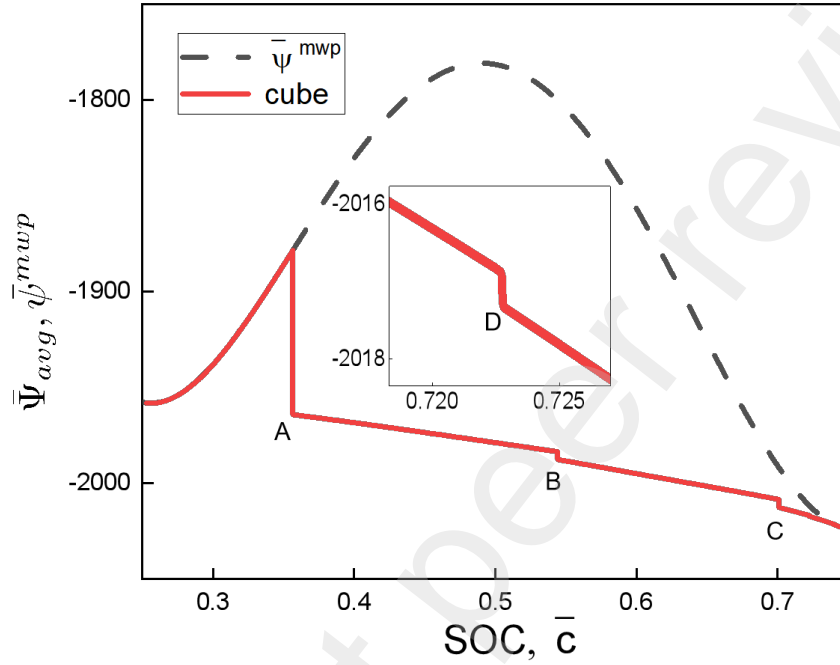
Fig. 2. Normalized average system free energy $\bar{\bar{\Psi}}_{avg}$ and, for comparison, normalized multiwell potential $\bar{\psi}^{mwp}$ as a function of SOC and $\bar{c}$, respectively, in a cube single-crystalline cathode particle of $Na_xV_2(PO_4)_3$.

As insertion proceeds, the sodium-rich cylindrical island expands along the other directions [100] and [010] (see SOC=50%). When the SOC gets close to 54.439%, $Na_xV_2(PO_4)_3$ displays the dynamics of single wave propagation, corresponding to the second "kink" B in Fig. 2. The phase boundary between $NaV_2(PO_4)_3$ and $Na_3V_2(PO_4)_3$ moves along [010], and a quasi-equilibrium intercalation-wave is formed with a warping of the interface, see

21

Fig. 4a.
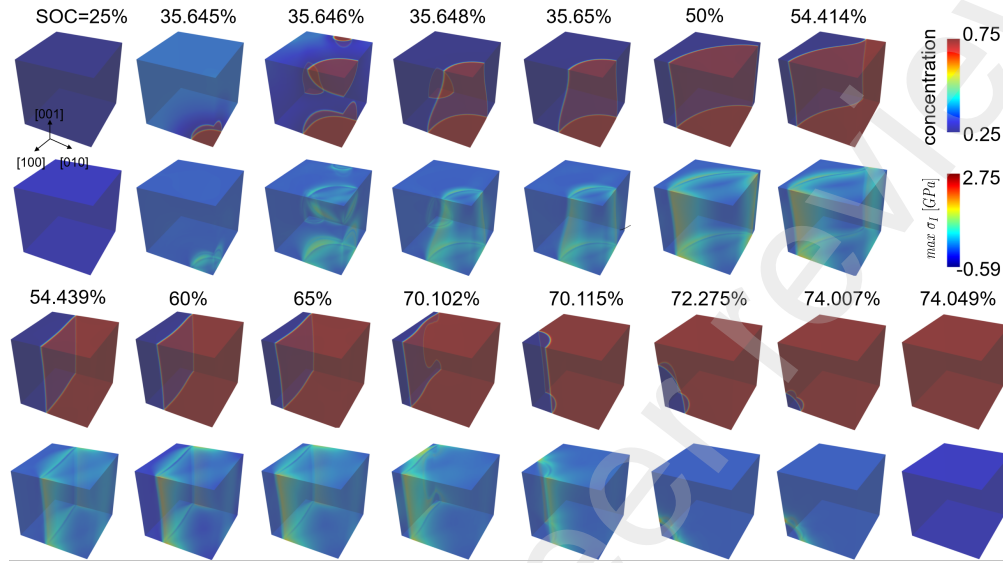
Fig. 3. Evolution of the 3D microstructure and the corresponding maximum principal stress σ_I as functions of SOC during sodium insertion in a cube single-crystalline cathode particle of $Na_xV_2(PO_4)_3$. For better visibility, iso-surface visualization is used.

The filling of Na ions goes head through the phase boundary motion until the intercalation-wave arrives at the other [010] facet, corresponding to the third "kink" C in Fig. 2. To minimize the total system free energy, a low concentration cylindrical island abruptly appears along [001], see SOC=70.115%. With the SOC approaching 72.275%, the high concentration phase $Na_3V_2(PO_4)_3$ immediately dominates all of the particle, corresponding to the fourth "kink" D in Fig. 2. Similar to the initial sodium-poor state $NaV_2(PO_4)_3$, the particle is stress-free for the final sodium-rich state $Na_3V_2(PO_4)_3$.

One remarkable aspect of microstructure evolution is that $Na_xV_2(PO_4)_3$

22

displays the dynamics of quasi-equilibrium single wave propagation along [010]. But why does the phase boundary move along this direction rather than other directions although Na ion intercalation happens equally at all particle surfaces? We point out that phase boundary motion along [010] is thermodynamically restricted by minimization of the coupling energy, which is determined by the anisotropic elasticity tensor. The anisotropic elasticity tensor favors phase boundary motion along [010] as it will not then introduce a phase boundary plane including the [010] axis along which the elasticity tensor component is largest. Another remarkable aspect of microstructure evolution is that, during the quasi-equilibrium states, the intercalation-wave always has a warping of the interface with a slight S shape rather than the traditional convex or concave phase boundary, for example, seen in the cathode material Na_xFePO_4 (Zhang et al., 2023).

As far as the mechanism underlying this interesting behavior is concerned, we note that the anti-orthotropic symmetry property of the elasticity tensor contributes to this striking behavior of warping of the interface of $Na_xV_2(PO_4)_3$. This is well verified through a control simulation, in which, we consider the orthotropic symmetric elasticity tensor, see Fig. 4. It is found that, in this control simulation without the anti-orthotropic symmetry property of the elasticity tensor, a concave interface is formed in Fig. 4b rather than a warping of the interface as seen with the original anti-orthotropic symmetric elasticity tensor shown in Fig. 4a. Thus, the anti-orthotropic symmetric elasticity tensor, with the non-vanishing elastic constants c_{16}, c_{26}, c_{36}, as well as c_{45}, makes the interface of $Na_xV_2(PO_4)_3$ warped.

23

55%   60%   65%

[010]
→ [100]

(a) anti-orthotropic symmetric elasticity tensor

(b) orthotropic symmetric elasticity tensor
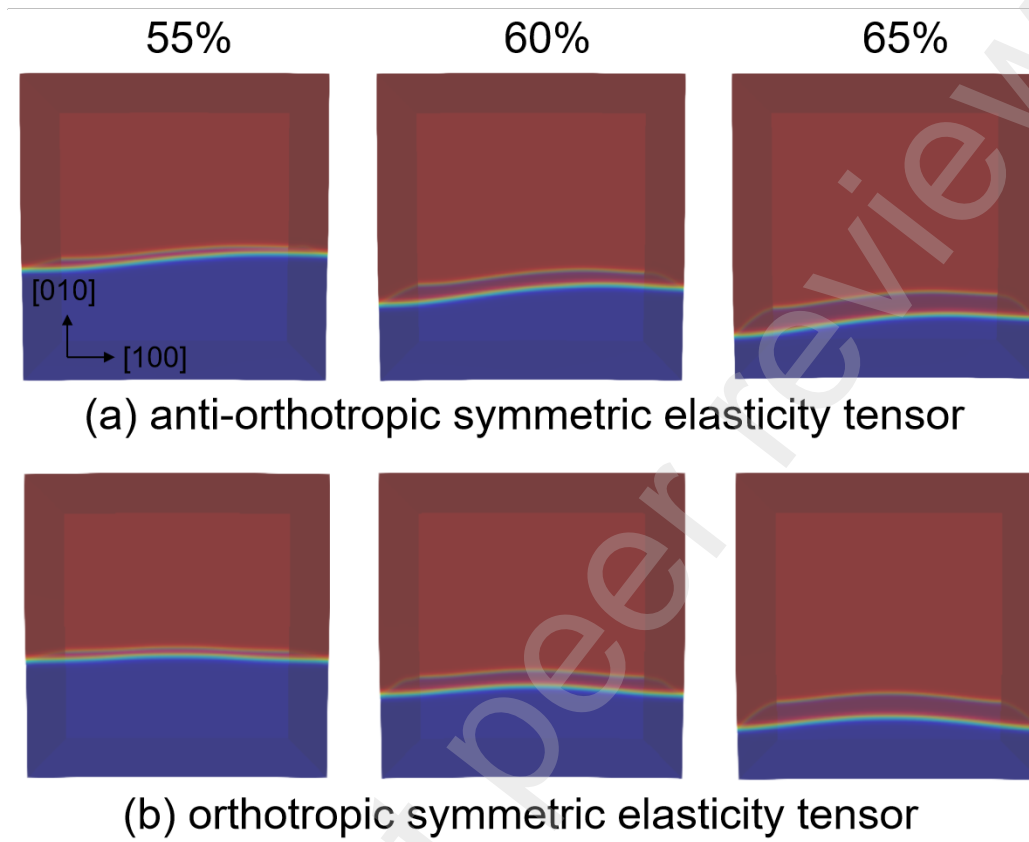
Fig. 4.   Effect of the anti-orthotropic symmetry property of the elasticity tensor of
$Na_xV_2(PO_4)_3$. (a) 3D microstructure at SOC=0.55, 0.6, 0.65 in a cube single-crystalline
cathode particle with the original anti-orthotropic symmetric elasticity tensor. (b) 3D microstructure at SOC=0.55, 0.6, 0.65 in a cube single-crystalline cathode particle assuming
the orthotropic symmetric elasticity tensor. For better visibility, iso-surface visualization
is used.

3.2. Influence of the crystal orientation

Here we study prismatic-like single-crystalline particles ($500nm \times 500nm \times 1000nm$) for three crystal orientations with the [100], [010], or [001] crystal
axes, respectively, being perpendicular to the small plane of the particle,

24

as shown in Fig. 5a. All of them share the same boundary conditions as the cube single-crystalline cathode particle. Fig. 5b shows the system free energy evolution of $Na_xV_2(PO_4)_3$ during insertion by the solid lines for the three prismatic-like single-crystalline particles, while the evolution of the 3D microstructure and the corresponding maximum principal stress, σ_I, is shown in Figs. 6 - 8. For comparison purposes, both, the dimensionless multiwell potential versus normalized concentration and the plot of the system free energy evolution for the cube single-crystalline cathode particle are also included in Fig. 5b.
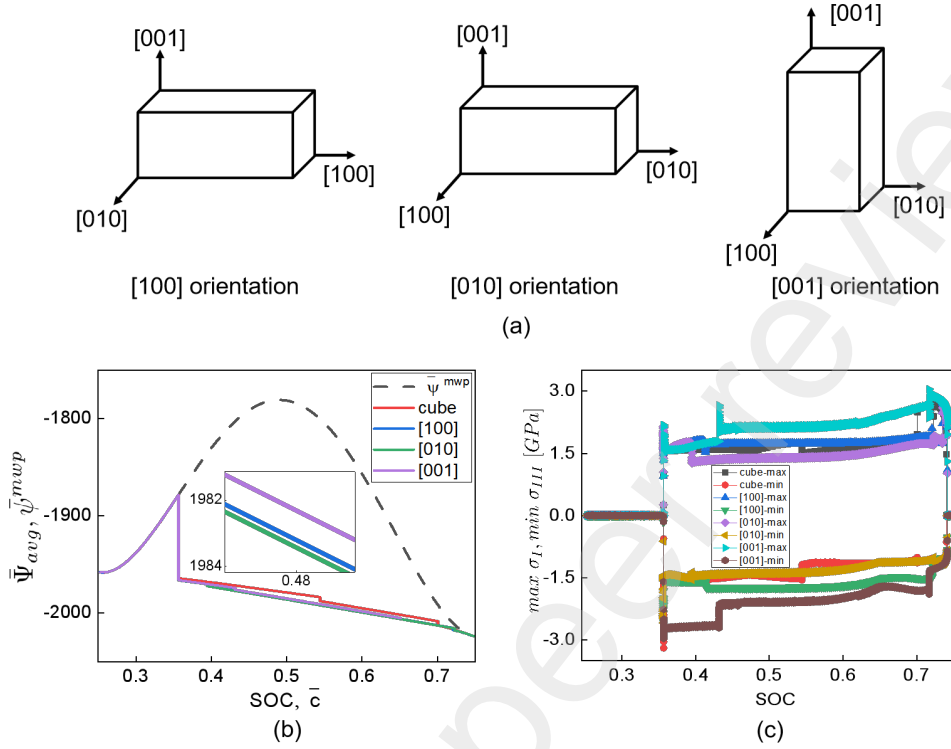
Fig. 5. (a) Prismatic-like single-crystalline cathode particles for three crystal orientations with the [100], [010], or [001] crystal axes, respectively, being perpendicular to the small plane of the particle. (b) Normalized average system free energy $\bar{\Psi}_{avg}$ and normalized multiwell potential $\bar{\psi}^{mwp}$ as functions of SOC and $\bar{c}$, respectively, for different single-crystalline cathode particles of $Na_xV_2(PO_4)_3$. (c) The highest value of the maximum principal stress $max\ \sigma_I$ and the lowest value of the minimum principal stress $min\ \sigma_{III}$ as functions of SOC for the different single-crystalline cathode particles of $Na_xV_2(PO_4)_3$.

First, we focus on the [100] crystal orientation case shown in Fig. 6. The high concentration phase $Na_3V_2(PO_4)_3$ first nucleates at the particle corner, and a sodium-rich island quickly appears along the [100] edge. Similar to the cube case, the anisotropic misfit strain leads to the abrupt ap-

26

pearance of a sodium-rich cylindrical island along [001], see SOC=35.64%. When the SOC approaches 41.58%, in contrast to the intercalation-wave along [010] from the cube case, $Na_xV_2(PO_4)_3$ displays the dynamics of single wave propagation along [100]. This is due to the fact that, in the presence of the [100] crystal orientation, the phase boundary between $NaV_2(PO_4)_3$ and $Na_3V_2(PO_4)_3$ moves along [100] to achieve a smaller interface region. This movement leads to a reduction in interface energy and consequently, a decrease in elastic strain energy, though it introduces a phase boundary plane including the [010] axis along which the elasticity tensor component is largest. Therefore, the phase boundary motion is thermodynamically affected by the crystal orientation, which is controlled by minimization of the interface area. During the single wave propagation period, similar to the cube case, the intercalation-wave still shows a warping of the interface due to the anti-orthotropic symmetry property of the elasticity tensor. Furthermore, single wave propagation along [100] in this case is less energetically expensive than that along [010] in the previous cube case, which can be verified by the plot of the system free energy shown in Fig. 5b. The filling of Na ions goes head through the phase boundary motion until the intercalation-wave arrives at the other [100] facet. At this point, a low concentration cylindrical island $NaV_2(PO_4)_3$ abruptly appears along [001] to minimize the total system free energy, see SOC=72.1%. When the SOC approaches 74.18%, the high concentration phase $Na_3V_2(PO_4)_3$ immediately dominates all of the particle, and it is stress-free for the final sodium-rich state $Na_3V_2(PO_4)_3$.

27
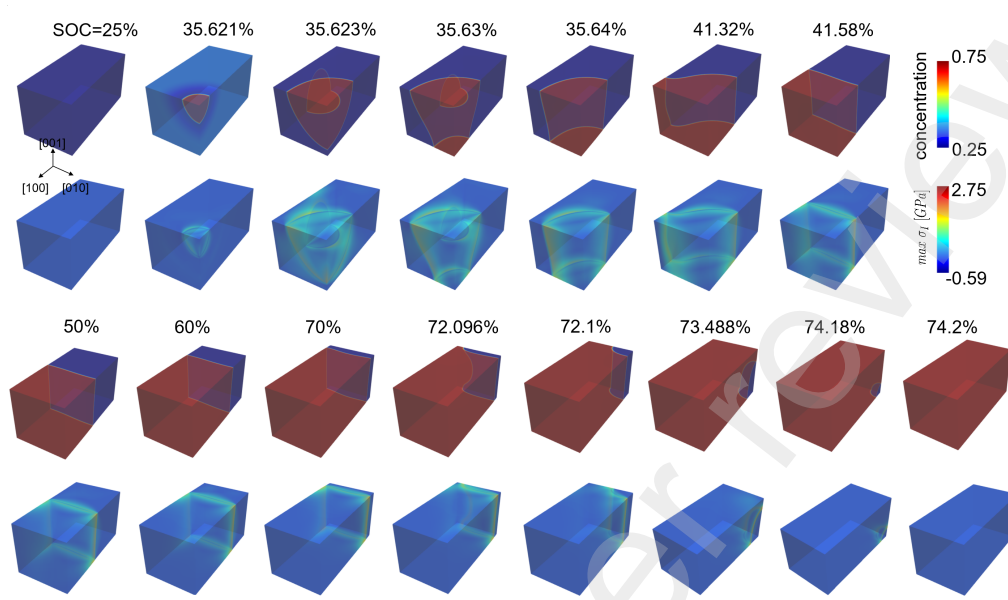
Fig. 6. Evolution of the 3D microstructure and the corresponding maximum principal stress σ_I as functions of SOC during sodium insertion in a prismatic-like single-crystalline cathode particle of $\mathrm{Na}_x\mathrm{V}_2(\mathrm{PO}_4)_3$ with the [100] crystal orientation. For better visibility, iso-surface visualization is used.

For the [010] crystal orientation case, as shown in Fig. 7, the high concentration phase $\mathrm{Na}_3\mathrm{V}_2(\mathrm{PO}_4)_3$ first nucleates at the particle corners, and the minimization of the total system free energy leads to the abrupt appearance of a sodium-rich cylindrical island along [001] due to the anisotropic misfit strain, see SOC=35.635%. When the SOC approaches 39.504%, $\mathrm{Na}_x\mathrm{V}_2(\mathrm{PO}_4)_3$ exhibits the dynamics of single wave propagation along [010] accompanied by a warping of the interface to minimize its area. The filling of Na ions goes head through the phase boundary motion until the intercalation-wave arrives at the other [010] facet, and a low concentration cylindrical island $\mathrm{NaV}_2(\mathrm{PO}_4)_3$ abruptly appears along [001] to minimize the total system free

28

energy, see SOC=72.328%. The high concentration phase $Na_3V_2(PO_4)_3$ immediately dominates all of the particle when the SOC approaches 74.18%.
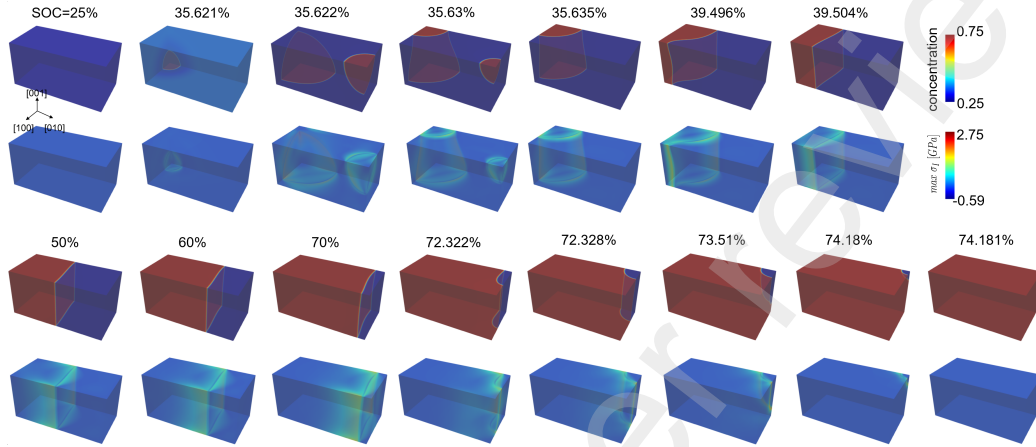
Fig. 7. Evolution of the 3D microstructure and the corresponding maximum principal stress σ_I as functions of SOC during sodium insertion in a prismatic-like single-crystalline cathode particle of $Na_xV_2(PO_4)_3$ with the [010] crystal orientation. For better visibility, iso-surface visualization is used.

As for the [001] crystal orientation case shown in Fig. 8, the high concentration phase $Na_3V_2(PO_4)_3$ first nucleates at the particle corners, and a sodium-rich island quickly appears along the [010] edge. However, during this very short nucleation period, the sodium-rich cylindrical island $Na_3V_2(PO_4)_3$ nucleates along [100] rather than [001], see SOC=35.685%. This is because the nucleation of a sodium-rich cylindrical island along [001] is not favored, as it would result in a much larger interface area. Instead, the anisotropic elasticity tensor induces the nucleation of $Na_3V_2(PO_4)_3$ along [100] as it will then introduce a phase boundary plane including the [100] axis along which the elasticity tensor component is smallest. As expected, $Na_xV_2(PO_4)_3$ exhibits

29

a quasi-equilibrium intercalation-wave along [001] due to the influence of the [001] crystal orientation. The phase boundary between $NaV_2(PO_4)_3$ and $Na_3V_2(PO_4)_3$ has a relatively flat interface aligned with [001] during single wave propagation. The filling of Na ions goes head through the phase boundary motion until the intercalation-wave arrives at the other [001] facet, and a low concentration cylindrical island $NaV_2(PO_4)_3$ abruptly appears along [100] to minimize the total system free energy, see SOC=71.703%. Among three crystal orientation cases, single wave propagation along [010] is most energetically favorable due to the synchronized effect of the crystal orientation and the elastic strain energy, which can be verified by the plot of the system free energy shown in Fig. 5b.
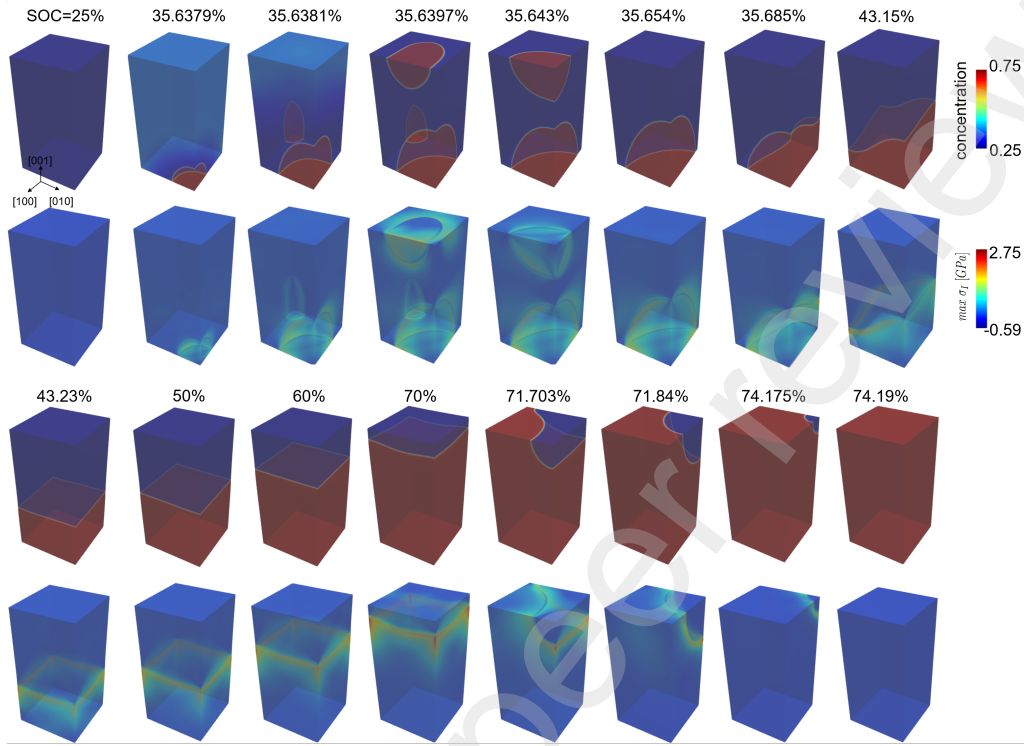
Fig. 8. Evolution of the 3D microstructure and the corresponding maximum principal stress σ_I as functions of SOC during sodium insertion in a prismatic-like single-crystalline cathode particle of $\text{Na}_x\text{V}_2(\text{PO}_4)_3$ with the [001] crystal orientation. For better visibility, iso-surface visualization is used.

Now we focus on the stresses in a $\text{Na}_x\text{V}_2(\text{PO}_4)_3$ particle during the insertion process for different crystal orientations, as shown in Fig. 5c. For comparison, the stress plots for the cube single-crystalline cathode particle are also included. In all cases, the maximum compressive stress magnitude is reached when phase nucleation is initiated, and the maximum tensile stress is reached at the end of phase segregation. Both, the highest magnitude of the maximum principal stress $max \ \sigma_I$ and the one of the minimum principal

31

stress $min\ \sigma_{III}$ are the largest in the [001] crystal orientation case but are the smallest in the [010] crystal orientation case. For example, the overall stress levels during the single wave propagation period in the whole particle of $Na_x V_2(PO_4)_3$ are much larger in the [001] crystal orientation case than those in the [010] crystal orientation case. In the [100] crystal orientation case, the overall stress levels are between the above two cases, and the tensile $max\ \sigma_I$ is similar to the cube one. As a result, the higher overall stress level in the [001] crystal orientation case indicates that such kinds of crystal orientation is more prone to particle fracture and mechanical degradation of $Na_x V_2(PO_4)_3$. On the other hand, the [010] crystal orientation in $Na_x V_2(PO_4)_3$ particles is mechanically more reliable, and, thus, recommended for the electrode design of $Na_x V_2(PO_4)_3$ in view of mechanical stability and consequently better battery performance.

4. Conclusions

A virtual multiscale modeling chain has been established to develop an anisotropic chemo-mechanical phase-field model based on first-principles calculations for $Na_x V_2(PO_4)_3$ of NIBs, accounting for diffusion, phase changes, anisotropic misfit strain, as well as anisotropic elasticity. DFT calculations indicate that $NaV_2(PO_4)_3$ shows the anti-orthotropic symmetry property of the elasticity tensor with a significantly larger elastic constant c_{22} compared to other elastic constants. The multiwell potential of $Na_x V_2(PO_4)_3$ is determined based on the experimental open circuit voltage for the first time. We study how elastic effects and crystal orientation influence 3D microstructure evolution, including phase evolution, interface morphology, and stress

evolution in $Na_xV_2(PO_4)_3$ particles.

Our simulations in a cube single-crystalline cathode particle predict the dynamics of quasi-equilibrium single wave propagation along [010], which is controlled by the anisotropic elasticity tensor. The anti-orthotropic symmetry property of the elasticity tensor induces the striking behavior of warping of the interface. We find that the phase boundary motion is thermodynamically affected by the crystal orientation. $Na_xV_2(PO_4)_3$ displays the dynamics of single wave propagation along [100], [010], and [001] to minimize the interface area, for the [100], [010], and [001] crystal orientation, respectively. It is demonstrated that the [001] crystal orientation in $Na_xV_2(PO_4)_3$ particles is more prone to particle fracture and mechanical degradation, and the [010] crystal orientation is mechanically more reliable.

More generally, the calculated elastic properties and constructed multi-well potential can provide significant input for the future study of $Na_xV_2(PO_4)_3$. Apart from yielding information about the properties of $Na_xV_2(PO_4)_3$, we envision that the findings of this work of the virtual multiscale modeling chain may point towards opportunities to optimize the crystal orientation of the phase separating electrode materials to achieve improved mechanical stability and consequently better battery performance.

Acknowledgments

Appendix A. Weak form of the boundary-value problem

We multiply the field equations (16), (20), and (21) with variational test functions δc, $\delta \mu$ and $\delta \vec{u}$ as used in Galerkin's method, and integrate over the full body. For the field equation (16) resulting from the mixed formulation, we obtain

$$
\begin{aligned}
G_c(c, \mu, \vec{u}) \;\; = \;\; & \int_{\mathcal{B}} dV \frac{\partial \psi^{mwp}}{\partial c} \delta c - \int_{\mathcal{B}} dV \frac{RT_{ref}}{c_{max}} \lambda \operatorname{div}(\operatorname{grad} c) \, \delta c \\
& + \int_{\mathcal{B}} dV \frac{\partial \psi^e}{\partial c} \, \delta c - \int_{\mathcal{B}} dV \mu \delta c = 0,
\end{aligned}
\tag{A.1}
$$

which depends on the displacement through the elastic strain energy density. Applying the divergence theorem and integration by parts, we rearrange the above weak form to

$$
\begin{aligned}
G_c(c, \mu, \vec{u}) \;\; = \;\; & \int_{\mathcal{B}} dV \frac{\partial \psi^{mwp}}{\partial c} \delta c + \int_{\mathcal{B}} dV \frac{RT_{ref}}{c_{max}} \lambda \operatorname{grad} c \cdot \operatorname{grad}(\delta c) \\
& + \int_{\mathcal{B}} dV \frac{\partial \psi^e}{\partial c} \, \delta c - \int_{\mathcal{B}} dV \mu \delta c \\
& - \int_{\partial \mathcal{B}} dA \frac{RT_{ref}}{c_{max}} \lambda \operatorname{grad} c \cdot \vec{n} \delta c = 0.
\end{aligned}
\tag{A.2}
$$

Following the same procedure for Equation (20), the balance of mass yields

$$
\begin{aligned}
G_\mu(\mu, c) \;\; = \;\; & \int_{\mathcal{B}} dV \frac{\partial c}{\partial t} \delta \mu + \int_{\mathcal{B}} dV c \mathbf{M}(c) \operatorname{grad} \mu \cdot \operatorname{grad}(\delta \mu) \\
& - \int_{\partial \mathcal{B}} dA c \mathbf{M}(c) \operatorname{grad} \mu \cdot \vec{n} \delta \mu.
\end{aligned}
\tag{A.3}
$$

It should be mentioned that, in order to improve the convergence, we use the equation describing the balance of mass to solve for the chemical potential rather than the concentration. The weak form of Equation (21) describing the balance of linear momentum reads

$$G_{\vec{u}}(\vec{u}, c) = \int_{\mathcal{B}} dV \mathbf{T} : \mathrm{grad}(\delta\vec{u}) - \int_{\partial\mathcal{B}} dA \mathbf{T} \cdot \vec{n} \cdot \delta\vec{u} = 0. \qquad (\mathrm{A.4})$$

The dependence of $G_{\vec{u}}(\vec{u}, c)$ on the concentration results from the definition of the stress tensor. Note that the parts related to surface integrals in Equations (A.2) and (A.4), respectively, drop out in the implementation due to the neglect of surface wetting (17) and due to traction free surfaces (23).

References

Afshar, A., Di Leo, C.V., 2021. A thermodynamically consistent gradient theory for diffusion–reaction–deformation in solids: Application to conversion-type electrodes. Journal of the Mechanics and Physics of Solids 151, 104368.

Akcay, T., Häringer, M., Pfeifer, K., Anhalt, J., Binder, J.R., Dsoke, S., Kramer, D., Mönig, R., 2021. $Na_3V_2(PO_4)_3$-A Highly Promising Anode and Cathode Material for Sodium-Ion Batteries. ACS Applied Energy Materials 4, 12688–12695.

Birkl, C.R., McTurk, E., Roberts, M., Bruce, P., Howey, D., 2015. A parametric open circuit voltage model for lithium ion batteries. Journal of The Electrochemical Society 162, A2271.

Bistri, D., Di Leo, C.V., 2023. A continuum electro-chemo-mechanical gradient theory coupled with damage: Application to Li-metal filament growth in all-solid-state batteries. Journal of the Mechanics and Physics of Solids 174, 105252.

Blöchl, P.E., 1994. Projector augmented-wave method. Physical Review B 50, 17953.

Buchholz, D., Moretti, A., Kloepsch, R., Nowak, S., Siozios, V., Winter, M., Passerini, S., 2013. Toward Na-ion Batteries—Synthesis and Characterization of a Novel High Capacity Na Ion Intercalation Material. Chemistry of Materials 25, 142–148.

Cahn, J.W., Hilliard, J.E., 1958. Free energy of a nonuniform system. i. interfacial free energy. The Journal of Chemical Physics 28, 258–267.

Chang, L., Lu, Y., He, L., Ni, Y., 2018. Phase field model for two-phase lithiation in an arbitrarily shaped elastoplastic electrode particle under galvanostatic and potentiostatic operations. International Journal of Solids and Structures 143, 73–83.

Cogswell, D.A., Bazant, M.Z., 2012. Coherency strain and the kinetics of phase separation in LiFePO$_4$ nanoparticles. ACS Nano 6, 2215–2225.

Deshpande, V.S., McMeeking, R.M., 2023. Models for the Interplay of Mechanics, Electrochemistry, Thermodynamics, and Kinetics in Lithium-Ion Batteries. Applied Mechanics Reviews 75, 010801.

Di Leo, C.V., Rejovitzky, E., Anand, L., 2014. A cahn–hilliard-type phase-field theory for species diffusion coupled with large elastic deformations:

36

application to phase-separating Li-ion electrode materials. Journal of the Mechanics and Physics of Solids 70, 1–29.

Di Leo, C.V., Rejovitzky, E., Anand, L., 2015. Diffusion–deformation theory for amorphous silicon anodes: the role of plastic deformation on electro-chemical performance. International Journal of Solids and Structures 67, 283–296.

Dou, X., Hasa, I., Saurel, D., Vaalma, C., Wu, L., Buchholz, D., Bresser, D., Komaba, S., Passerini, S., 2019. Hard carbons for sodium-ion batteries: Structure, analysis, sustainability, and electrochemistry. Materials Today 23, 87–104.

Du, K., Guo, H., Hu, G., Peng, Z., Cao, Y., 2013. $Na_3V_2(PO_4)_3$ as cathode material for hybrid lithium ion batteries. Journal of power sources 223, 284–288.

Euchner, H., Groß, A., 2022. Atomistic modeling of Li-and post-Li-ion bat-teries. Physical Review Materials 6, 040302.

Ganser, M., Hildebrand, F.E., Kamlah, M., McMeeking, R.M., 2019. A finite strain electro-chemo-mechanical theory for ion transport with application to binary solid electrolytes. Journal of the Mechanics and Physics of Solids 125, 681–713.

Gaston, D., Newman, C., Hansen, G., Lebrun-Grandie, D., 2009. MOOSE: A parallel computational framework for coupled systems of nonlinear equa-tions. Nuclear Engineering and Design 239, 1768–1778.

Hohenberg, P., Kohn, W., 1964. Inhomogeneous electron gas. Physical Review 136, B864.

Hörmann, N.G., Groß, A., 2019. Phase field parameters for battery compounds from first-principles calculations. Physical Review Materials 3, 055401.

Huang, P., Gao, L.T., Guo, Z.S., 2022. Elastoplastic model for chemomechanical behavior of porous electrodes using image-based microstructure. International Journal of Solids and Structures 254, 111903.

Huang, P., Guo, Z.S., 2024. Framework for electrochemical-mechanical behavior of all-solid-state batteries: From the reconstruction method to multi-physics and multi-scale modeling. International Journal of Solids and Structures 305, 113078.

Jian, Z., Han, W., Lu, X., Yang, H., Hu, Y.S., Zhou, J., Zhou, Z., Li, J., Chen, W., Chen, D., et al., 2013. Superior electrochemical performance and storage mechanism of $Na_3V_2(PO_4)_3$ cathode for room-temperature sodium-ion batteries. Advanced Energy Materials 3, 156–160.

Jian, Z., Yuan, C., Han, W., Lu, X., Gu, L., Xi, X., Hu, Y.S., Li, H., Chen, W., Chen, D., et al., 2014. Atomic structure and kinetics of NASICON $Na_xV_2(PO_4)_3$ cathode for sodium-ion batteries. Advanced Functional Materials 24, 4265–4272.

Jian, Z., Zhao, L., Pan, H., Hu, Y.S., Li, H., Chen, W., Chen, L., 2012. Carbon coated $Na_3V_2(PO_4)_3$ as novel electrode material for sodium ion batteries. Electrochemistry Communications 14, 86–89.

38

Jiang, C., Zhong, Z., 2023. A thermo-electro-chemo-mechanically coupling theory considering species diffusion and electrochemical reaction. International Journal of Solids and Structures 267, 112147.

Klinsmann, M., Rosato, D., Kamlah, M., McMeeking, R.M., 2016a. Modeling crack growth during Li extraction and insertion within the second half cycle. Journal of power sources 331, 32–42.

Klinsmann, M., Rosato, D., Kamlah, M., McMeeking, R.M., 2016b. Modeling crack growth during Li insertion in storage particles using a fracture phase field approach. Journal of the Mechanics and Physics of Solids 92, 313–344.

Kohn, W., Sham, L.J., 1965. Self-consistent equations including exchange and correlation effects. Physical Review 140, A1133.

Kresse, G., Furthmüller, J., 1996. Efficient iterative schemes for ab initio total-energy calculations using a plane-wave basis set. Physical Review B 54, 11169.

Kresse, G., Hafner, J., 1993. Ab initio molecular dynamics for liquid metals. Physical Review B 47, 558.

Kresse, G., Joubert, D., 1999. From ultrasoft pseudopotentials to the projector augmented-wave method. Physical Review B 59, 1758.

Li, Y., Mao, W., Zhang, K., Yang, F., 2019. Analysis of large-deformed electrode of lithium-ion battery: Effects of defect evolution and solid reaction. International Journal of Solids and Structures 170, 1–10.

Lim, S.Y., Kim, H., Shakoor, R., Jung, Y., Choi, J.W., 2012. Electrochemical and thermal properties of NASICON structured $Na_3V_2(PO_4)_3$ as a sodium rechargeable battery cathode: a combined experimental and theoretical study. Journal of The Electrochemical Society 159, A1393.

Pandit, B., Johansen, M., Susana Martínez-Cisneros, C., Naranjo-Balseca, J.M., Levenfeld, B., Ravnsbæk, D.B., Varez, A., 2024. $Na_3V_2(PO_4)_3$ Cathode for Room-Temperature Solid-State Sodium-Ion Batteries: Advanced In Situ Synchrotron X-ray Studies to Understand Intermediate Phase Evolution. Chemistry of Materials 36, 2314–2324.

Perdew, J.P., Burke, K., Ernzerhof, M., 1996. Generalized gradient approximation made simple. Physical Review Letters 77, 3865.

Redlich, O., Kister, A., 1948. Activity coefficient model. Ind Eng Chem 24, 345–52.

Song, W., Ji, X., Wu, Z., Zhu, Y., Yang, Y., Chen, J., Jing, M., Li, F., Banks, C.E., 2014. First exploration of Na-ion migration pathways in the NASICON structure $Na_3V_2(PO_4)_3$. Journal of Materials Chemistry A 2, 5358–5362.

Stüble, P., Müller, C., Klemens, J., Scharfer, P., Schabel, W., Häringer, M., Binder, J.R., Hofmann, A., Smith, A., 2024. Enabling long-term cycling stability of $Na_3V_2(PO_4)_3/C$ vs. hard carbon full-cells. Batteries & Supercaps 7, e202300375.

Vaalma, C., Buchholz, D., Weil, M., Passerini, S., 2018. A cost and resource analysis of sodium-ion batteries. Nature reviews materials 3, 1–11.

Wang, B., Réthoré, J., Aifantis, K.E., 2021. Capturing the stress evolution in electrode materials that undergo phase transformations during electrochemical cycling. International Journal of Solids and Structures 224, 111032.

Wang, L., Maxisch, T., Ceder, G., 2006. Oxidation energies of transition metal oxides within the GGA + U framework. Physical Review B 73, 195107.

Xu, R., Yang, Y., Yin, F., Liu, P., Cloetens, P., Liu, Y., Lin, F., Zhao, K., 2019. Heterogeneous damage in Li-ion batteries: Experimental analysis and theoretical modeling. Journal of the Mechanics and Physics of Solids 129, 160–183.

Zhang, K., Li, Y., Wang, F., Zheng, B., Yang, F., Lu, D., 2020. An analytical model for lithiation-induced concurrent plastic flow and phase transformation in a cylindrical silicon electrode. International Journal of Solids and Structures 202, 87–98.

Zhang, T., Kamlah, M., 2018a. A nonlocal species concentration theory for diffusion and phase changes in electrode particles of lithium ion batteries. Continuum Mechanics and Thermodynamics 30, 553–572.

Zhang, T., Kamlah, M., 2018b. Sodium ion batteries particles: Phase-field modeling with coupling of cahn-hilliard equation and finite deformation elasticity. Journal of The Electrochemical Society 165, A1997–A2007.

Zhang, T., Kamlah, M., 2019. Phase-field modeling of the particle size and average concentration dependent miscibility gap in nanoparticles of

$Li_xMn_2O_4$, Li_xFePO_4, and Na_xFePO_4 during insertion. Electrochimica Acta 298, 31–42.

Zhang, T., Kamlah, M., 2020. Mechanically coupled phase-field modeling of microstructure evolution in sodium ion batteries particles of Na_xFePO_4. Journal of The Electrochemical Society 167, 020508.

Zhang, T., Kamlah, M., 2021. Microstructure evolution and intermediate phase-induced varying solubility limits and stress reduction behavior in sodium ion batteries particles of Na_xFePO_4 $(0 < x < 1)$. Journal of Power Sources 483, 229187.

Zhang, T., Kamlah, M., McMeeking, R.M., 2024a. Modeling storage particle delamination and electrolyte cracking in cathodes of solid state batteries. Journal of the Mechanics and Physics of Solids 185, 105551.

Zhang, T., Sotoudeh, M., Groß, A., McMeeking, R.M., Kamlah, M., 2023. 3D microstructure evolution in Na_xFePO_4 storage particles for sodium-ion batteries. Journal of Power Sources 565, 232902.

Zhang, T., Zhang, D., Balakrishna, A.R., 2024b. Coupling diffusion and finite deformation in phase transformation materials. Journal of the Mechanics and Physics of Solids 183, 105501.